LAWRENCE
LIVERMORE
NATIONAL
LABORATORY

LLNL-JRNL-638539

Quantitative Phase Composition of TiO2-Coated Nanoporous-Au Monoliths by X-ray Absorption Spectroscopy and Correlations to Catalytic Behavior

M. Bagge-Hansen, A. Wichmann, A. Wittstock, J. R. I. Lee, J. Ye, T. M. Willey, J. Biener, T. van Buuren, M. Baumer, M. Biener

June 6, 2013

The Journal of Physical Chemistry C

Disclaimer

Quantitative Phase Composition of TiO_2-Coated Nanoporous-Au Monoliths by X-ray Absorption Spectroscopy and Correlations to Catalytic Behavior

Michael Bagge-Hansen,[1]* Andre Wichmann,[2] Arne Wittstock,[2] Jonathan R. I. Lee,[1] Jianchao Ye,[1] Trevor M. Willey,[1] Juergen Biener,[1] Tony van Buuren,[1] Marcus Bäumer,[2] and Monika Biener[1]

[1]*Physical and Life Sciences Directorate, Condensed Matter and Materials Division, Lawrence Livermore National Laboratory, 7000 East Ave., Livermore, CA 94550*

[2] *University Bremen, Centre for Environmental Research and Sustainable Technology and Institute of Applied and Physical Chemistry, Leobener Strasse NW2, 28359 Bremen, Germany*

*Address correspondence to *baggehansen1@llnl.gov*

***Abstract**:*

Porous titania/metal hybrid materials have many potential applications in the fields of green catalysis, energy harvesting and storage in which both the crystallographic phase of the titania (TiO_2) component and the overall morphology of the nanoporous hybrid material determine the material's performance. Near-edge x-ray absorption fine structure (NEXAFS) spectroscopy provides quantitative crystallographic phase composition from ultrathin, nanostructured titania films, including sensitivity to amorphous regions, yielding new insights into the structure-function relationships of these materials. Here, we report on the effects of annealing temperature on crystallographic phase, morphology and catalytic activity of titania functionalized nanoporous gold (np-Au). The material was prepared by atomic layer deposition of titania on millimeter-sized samples of np-Au. Aerobic CO oxidation was used as a model reaction for catalytic activity. The annealing induced changes in catalytic activity are correlated with concurrent morphology and phase changes as provided by cross-sectional scanning electron microscopy, transmission electron microscopy and NEXAFS spectroscopy.

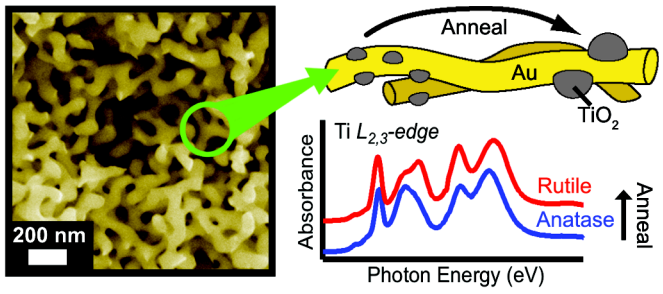

KEYWORDS: nanoporous gold, titania, NEXAFS, atomic layer deposition, catalysis, phase, morphology

Surface functionalized bulk nanoporous materials—such as nanoporous gold (np-Au)—are poised to deliver significant impact in the fields of green catalysis, energy harvesting and storage.[1-5] The superior performance of these very high surface area, nanoporous materials is achieved by optimizing surface-dominated interactions through rational design and synthetic control of the configuration and chemical composition of the exposed surfaces. To fully leverage this strategy, a comprehensive description of the material surface structure is essential for identifying the underlying structure-function relationships. In this study, near-edge x-ray absorption fine structure (NEXAFS) spectroscopy provides unprecedented fidelity for the structural characterization of incrementally annealed, ultrathin, nanostructured titania films deposited on np-Au—yielding new insights into the sensitivity of catalytic behavior to various structural polymorphs, their corresponding morphology and the possibility of exploiting these relationships to maximize performance.

Atomic layer deposition (ALD) is an elegant and generally effective strategy for functionalization of high surface area bulk nanoporous materials.[6, 7] In particular, ALD offers precise control of surface composition on all exposed surfaces, including the interior walls of nanopores, by virtue of its self-limiting deposition mechanism. Titania (TiO_2), for which a robust ALD process exists, is among the most versatile candidate materials for functionalization of nanoporous metals as it can be used to add catalytic, photocatalytic, and Li ion storage functionalities.[8-10] In TiO_2/metal hybrid materials, the activity of the TiO_2 coating is influenced by the nanoporous metal substrate through, for example, strong metal support interaction (SMSI) effects, plasmonic effects[11], or provision of a metallic backbone for efficient current collection in energy harvesting and storage applications.[12] In particular, the interface between metal oxides (*i.e.,* TiO_2) and Au have demonstrated a synergistic chemical effect, dramatically augmenting the dissociative adsorption, and thus chemical activation, of molecular oxygen.[13] This effect is of profound importance to the catalytic activity of these materials as dissociation of molecular oxygen is a strongly limiting step: *e.g.,* in low temperature aerobic oxidation of CO. Access to the critical TiO_2/Au interface by O_2 impinging on the surface is provided only at the perimeter of surface deposits. It has recently been demonstrated that TiO_2 functionalized np-Au has astonishing activity and stability for the aerobic oxidation of CO as well as the reduction of NO, both of which are crucial reactions in exhaust gas treatment.[14]

Np-Au is a prominent bulk nanoporous material that has attracted intensive research efforts, providing encouraging results as a catalyst, actuator and sensor.[15-17] The material can easily be prepared by corrosion of Au-Ag alloys, and has a characteristic bicontinuous structure of interconnected gold ligaments and pores. The characteristic feature size of the as-prepared material is 40-50 nm, and the specific surface area is ~3.6 m^2/g.[18] Significantly, np-Au is readily coated by ALD with conformal films of TiO_2.[19] Generally, titania may be present in either amorphous form or in any of the three crystalline phases—anatase, brookite, and rutile. Low temperature ALD of TiO_2 typically results in the formation of continuous amorphous TiO_2 coatings. Further thermal processing can induce recrystallization and systematic changes in morphology (*e.g.,* through beading, coalescence, sintering, or Ostwald ripening). In these annealed TiO_2/np-Au materials, TiO_2 crystallites are found uniformly distributed across the np-Au surface, presenting substantial exposed TiO_2/Au interface for enhanced dissociative adsorption of O_2. It has also been reported that the catalytic activity of Au nanoparticles supported on TiO_2 is strongly influenced by crystalline phase.[20] Given these features, it is likely that crystallite size, shape, and coverage are intimately related to the crystallographic phase. Therefore, precise control of both phase and morphology could offer significant gains by tuning these highly coupled parameters to maximize performance; however, to-date this approach has not been fully leveraged, in part, due to a lack of quantitative characterization.

The three crystalline phases of TiO_2 share the same structural motif of TiO_6 octahedra; though, they differ in how the TiO_6 units are connected to each other—and therefore the degree of distortion of the TiO_6 octahedra.[21-23] In rutile, the TiO_6 units form edge connected TiO_6 ribbons while in anatase, each TiO_6 unit has four edge connections. These polymorphs can be easily discerned in bulk samples of TiO_2 by x-ray diffraction (XRD) or Raman spectroscopy; however, both techniques fail to detect amorphous TiO_2. In the case of TiO_2/metal hybrid materials, where TiO_2 is only present in minute amounts, sensitivity presents an

additional challenge. These deficiencies suggest less traditional techniques are needed for quantitative phase characterization of TiO_2/metal hybrid nanoporous materials.

Synchrotron-based NEXAFS spectroscopy is an element specific technique that is (1) very sensitive to changes in the local bonding environment and (2) readily applied to samples containing only trace quantities. Moreover, the Ti NEXAFS $L_{2,3}$-edge is well known to exhibit exceptional sensitivity to Ti coordination and structure.[24-31] For example, amorphous TiO_2 and anatase and rutile polymorphs of TiO_2 can be clearly distinguished (see *e.g.,* Kucheyev, *et al.*[26]) by comparison of both peak positions and line-shape, especially in the fine structure of the e_g-band of the L_3-edge.[24-26] NEXAFS is, therefore, an ideal tool to characterize and quantify the phase composition of TiO_2 ALD thin films used in the functionalization of bulk nanoporous materials.

In this study, we report variations in the catalytic activity of TiO_2/np-Au with post-ALD annealing. The as-deposited ALD TiO_2 is amorphous; however, annealing to temperatures <1300 K induces controlled recrystallization and thus the ability to specify the predominant TiO_2 phase and morphology on the np-Au support. NEXAFS spectroscopy, cross-sectional scanning electron microscopy (xSEM), and transmission electron microscopy (TEM) provided unprecedented resolution for the systematic study of these changes in morphology and TiO_2 phase composition. Aerobic CO oxidation of annealed TiO_2/np-Au samples was used as a model reaction to explore the structure-function relationship between observed variation in catalytic activity and annealing induced morphology and crystallographic phase changes.

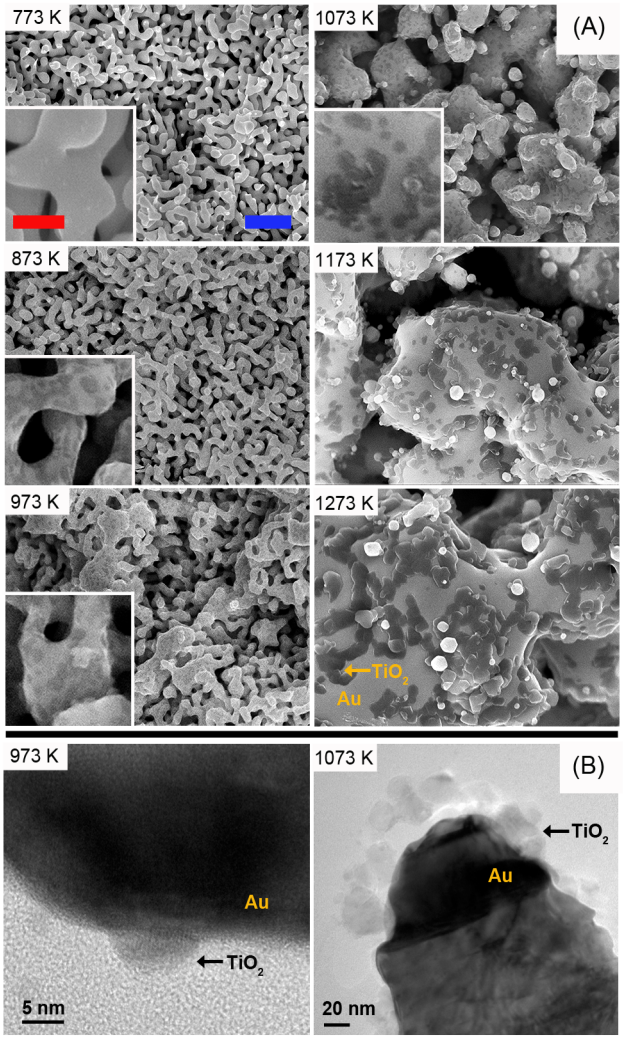

Figure 1: (A) Scanning electron micrographs of cross sections of TiO_2/np-Au disks annealed at temperatures from 773 – 1273 K. The images are shown in constant magnification (blue scale bar = 500 nm) with higher magnification insets (red scale bar = 100 nm) for details of the TiO_2 film morphology. The TiO_2 film breaks up between 773 and 873 K. The Au ligaments are stable to >873 K; however, at annealing temperature in excess of 973 K, the mean Au ligament size increases rapidly with increasing temperature. Larger TiO_2 crystallites (dark grey regions) are more clearly observed with increasing annealing temperature. **(B)** Representative transmission electron micrographs at 973 and 1073 K: mean crystallite radius is observed to increase from ~10 nm to ~30 nm.

Results and Discussion:

The effect of post-deposition annealing on the morphology of the TiO_2/np-Au hybrid material is shown in Figure 1A by a series of representative cross-sectional scanning electron micrographs. As previously reported, after 30 cycles of TiO_2 ALD at 383 K, the surface of np-Au is coated with a conformal, ~2-nm-thick, continuous TiO_2 thin film.[14, 19] Annealing up to 873 K only slightly increases the characteristic feature size of np-Au as the TiO_2 deposit suppresses the coarsening of the Au ligaments that is typically observed through stress-assisted surface diffusion. At ~873 K, the initially continuous TiO_2 thin film is largely converted into discrete TiO_2 particles, resulting in a reduced stabilization of the np-Au structure. Consequently, the Au ligaments of TiO_2/np-Au start to coarsen, yet the rate of coarsening is not as fast as observed in uncoated np-Au due to step-edge pinning by TiO_2.[19, 32] Transmission electron micrographs are shown in Figure 1B for TiO_2/np-Au samples annealed to 973 and 1073 K; these representative data correlate well with the xSEM data and confirm that the size of discrete TiO_2 crystallites is a strong function of annealing temperature.

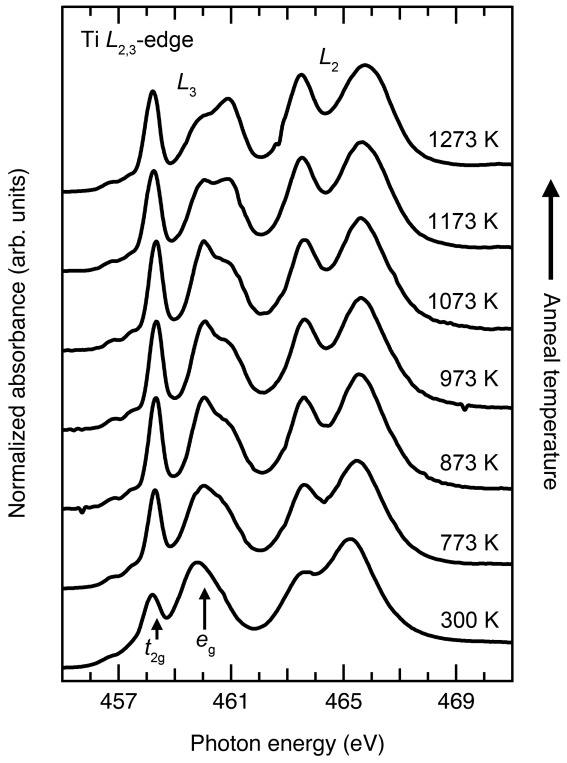

Figure 2: Ti $L_{2,3}$-edge spectra of TiO_2/npAu annealed to increasing temperatures from 773 to 1273 K in comparison to as-deposited TiO_2/npAu. Note the variation, especially in the e_g-band of the L_3-edge, indicative of phase changes between various TiO_2 polymorphs.

Post-deposition annealing induced TiO_2 phase changes in the ALD thin films were monitored by NEXAFS spectroscopy. Quantitative phase composition was obtained by applying the so-called "building block" interpretation of NEXAFS[33] that involves fitting of the Ti $L_{2,3}$-edge NEXAFS spectra shown in Figure 2 to linear combinations of Ti $L_{2,3}$-edge spectra obtained from amorphous TiO_2, anatase, and rutile reference samples. The validity of this approach relies on the following assumptions: (1) Ti $L_{2,3}$-edge spectra of TiO_2 polymorphs are sufficiently distinct to merit analysis of mixed phase samples by separation of the superimposed components, (2) amorphous, anatase, and rutile phases form a sufficient basis set, with no motivation to infer the presence of other phases (see supporting information), (3) stoichiometry is preserved, and (4) morphology changes associated with recrystallization of the thin film do not strongly affect the volume probed by NEXAFS. A chi-square minimization algorithm was implemented to select the best fit (see supporting information, S.1). Across the sample series, the linear combination fits are remarkably well correlated with the acquired Ti $L_{2,3}$-edge spectra (despite the constraints of the above assumptions), providing confidence that this approach captures the relative changes in composition. Further, results differ by no more than 5% at each intermediate temperature whether initial spectra were normalized to the step edge or overall peak intensity. Thus, it is then reasonable that the normalized coefficients of each best-fit linear combination correspond to the relative TiO_2 phase composition; these results are shown in Figure 3.

In addition to NEXAFS spectroscopy, more traditional techniques for the structural characterization of TiO_2, specifically Raman spectroscopy and XRD, were also used to interrogate a series of annealed TiO_2/np-Au samples (see supporting information). Significantly, analysis of the collected Raman spectra (S.I.2) provided highly corroborative results for our NEXAFS study; however, these Raman data provided neither quantitative phase composition, nor sensitivity for the amorphous phase that was available with NEXAFS spectroscopy. Meanwhile, examination of the XRD data (S.I.3) provided no indication of peaks associated with a crystalline TiO_2 thin film.

The NEXAFS analysis reveals that after annealing to 773 K almost half of the initially present amorphous TiO_2 film is already converted to anatase and some rutile. For comparison, amorphous TiO_2 gels start to crystallize to anatase at 643 K.[34] As the annealing temperature for TiO_2/np-Au is increased, the anatase content increases, until the maximum anatase content (~75 %) is reached after annealing to ~973 K. The rutile content, on the other hand, stays roughly constant at 15-20 % between 773 and 1073 K. At annealing temperatures of 1173 K and above, rutile suddenly becomes the predominant phase as the anatase component rapidly diminishes. This suggests that, at these higher annealing temperatures, rutile supplants anatase as the most thermodynamically stable configuration, in agreement with the bulk phase diagram.[35] It is interesting to note that while 90% of the initially present amorphous phase crystallizes at or below 973 K, the remaining 10% persists up to 1175 K over a region where rapid conversion from anatase to rutile is also observed. The crystallization resistant amorphous TiO_2 may thus be related to interfacial or intergranular material.

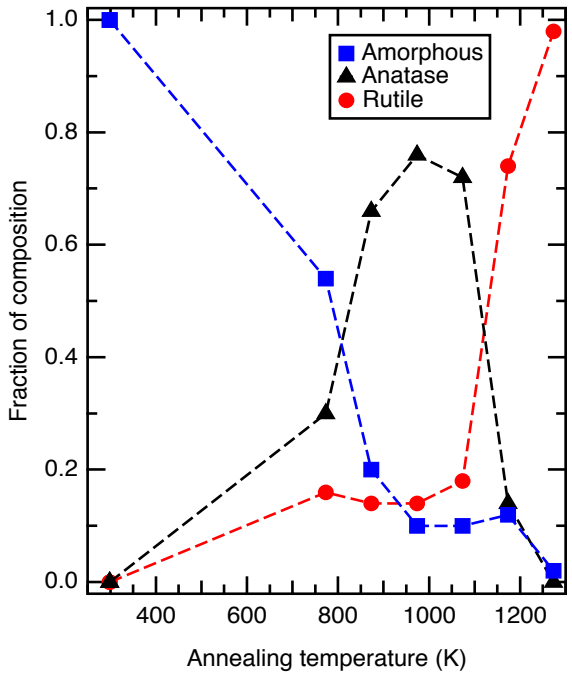

Figure 3: Relative phase composition of TiO_2/np-Au as a function of increasing post-deposition annealing temperature. Composition was determined by linear combination fitting of Ti $L_{2,3}$-edge spectra (for fitting output, see S.I. 1). Note an increasing anatase component is observed to reach a maxima at ~973 K.

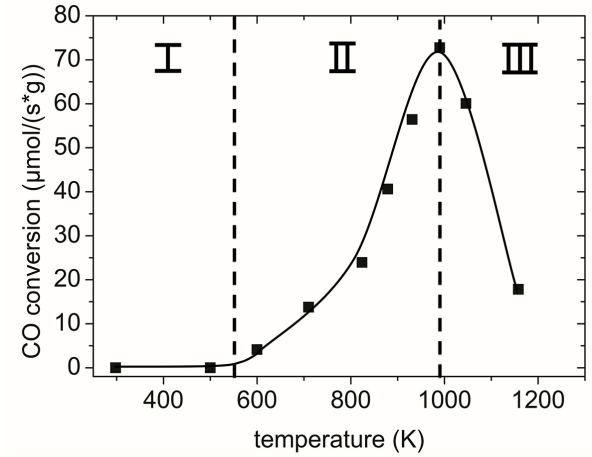

Figure 4: Effect of post-deposition annealing temperature on the catalytic activity of TiO_2/np-Au for CO oxidation (12 vol% CO, 30 vol% O_2, He balanced) at 333 K. Note the maxima in catalytic efficiency is observed for samples annealed to ~973 K.

These observations from NEXAFS spectroscopy are consistent with the reported size-dependent thermodynamic stabilities of anatase and rutile that are caused by the very different surface enthalpies of these two TiO_2 phases.[29, 36-39] While rutile represents the thermodynamically most stable bulk phase of TiO_2, anatase crystallites smaller than ~14 nm are stabilized by the lower surface enthalpy of this phase.[39] At higher annealing temperatures, as the TiO_2 nanocrystallites grow through coalescence, sintering, and/or Ostwald ripening, the lower surface enthalpy of anatase starts to lose its stabilizing effect, and the rutile becomes the thermodynamically more stable phase. Coarsening-induced anatase to rutile phase transformations are typically observed in the 900-1100 K regime.[29, 36, 37, 39]

The observation of ~15% rutile phase after only annealing to 773 K may thus be associated with the largest crystallites in the tail of the initial TiO_2 crystallite size distribution. New crystals formed by break up of the continuous, as-deposited film, in the annealing regime of 773 to ~1000 K, probably start small and thus are preferentially anatase. As they grow in size and decrease in number with increasing annealing temperature (*e.g.,* through coalescence, sintering, and/or Ostwald ripening) they transform into rutile. Although the literature cited here examine only powdered TiO_2, it is reasonable that qualitatively similar behavior occurs within ultrathin TiO_2 films on a Au surface, though it should be expected that the effect of the TiO_2/Au interface may influence the crystallite size at which the anatase to rutile phase transition becomes favorable. The xSEM and TEM data (Fig. 1) supports this analysis, with dramatically increasing crystallite size readily apparent with increasing annealing temperature from 973 - 1273 K. After annealing to 1273 K, typical faceted TiO_2 crystallites are ~150 nm in diameter.

The annealing induced morphology and phase changes discussed above dramatically affect the catalytic activity of the TiO_2/np-Au hybrid material. This is demonstrated in Figure 4 for aerobic CO oxidation (CO + ½ O_2 → CO_2). For purposes of discussion, we delineate three regions, distinguished by the effect of annealing temperature on catalytic performance: (I) the low temperature region in which no catalytic activity is observed, (II) the intermediate temperature region from 600 to 1000 K in which onset and increasing activity occurs, and (III) the high temperature region, above 1000 K, where precipitous loss of activity ensues.

For annealing temperatures below ~550 K (region I in Fig.4), no catalytic activity is observed for TiO_2/np-Au; in contrast, uncoated np-Au is catalytically active. As suggested by previous experiments, under similar conditions, ALD of TiO_2 leads to the formation of a continuous coating that completely covers the surface of the Au ligaments.[14, 19] Bulk TiO_2 is inactive for the aerobic oxidation of CO,[21] although very thin

(few monolayer) oxide films on metal substrates can become catalytically active in the presence of SMSI effects.[40] Here, the inactivity of TiO_2/np-Au samples annealed in the low temperature regime (I) confirms that the as-deposited, ~2 nm thick, TiO_2 coating provides complete, conformal coverage of the np-Au and SMSI effects are not present.

The TiO_2/np-Au hybrid material becomes catalytically active after annealing to 550 K (region II in Fig. 4), and the activity increases with increasing annealing temperature up to ~1000 K. At these temperatures, the initially continuous TiO_2 film gradually breaks up into discrete TiO_2 particles (*e.g.,* compare Fig.1 at 773 K and 873 K). Concomitantly, TiO_2 crystallization occurs; most notably, the fraction of anatase increases dramatically with increasing annealing temperature, from ~30 % at 773 K to ~80 % at 973 K (Fig. 3). The maximum activity of 75 μmol CO s^{-1} g^{-1} is reached at 973 K, which coincides almost exactly with the maximum fraction of anatase. As mentioned above, the formation of predominantly anatase TiO_2 in this temperature regime (II) suggests that the crystallites are ~1-14 nm in size: the xSEM and TEM data (Fig. 1) support this assertion. Therefore, it is reasonable to infer that a large fraction of necessarily small anatase crystallites provides the maximum exposed interface between the TiO_2 coating and the Au support (around the periphery of each TiO_2 crystallite), which provides enhanced dissociative adsorption of O_2,[13] and thus coincides with the greatest observed catalytic activity.

For annealing temperatures above ~1000 K (region III in Fig. 4), coarsening of Au ligaments proceeds rapidly. Consequently, the average pore diameter increases, improving conductivity for reactants and increasing the total active area. Nonetheless, catalytic activity is observed to rapidly decrease. The NEXAFS analysis shows that, over this same temperature regime, the TiO_2 crystallites undergo a phase transformation from anatase to rutile. The combined NEXAFS, xSEM and TEM data, suggest that this anatase-rutile phase transformation is an indicator for TiO_2 crystallite coarsening (> 14 nm diameter). The according loss of exposed TiO_2/Au interface at the crystallite perimeter is probably responsible for the observed decrease in catalytic activity. Only based on the xSEM data which indicates over an order of magnitude increase in crystallite radius, the corresponding catalytic activity should drop approximately 100-fold—much more than the observed ~10x (based on a simple geometrical assessment; see supporting information). While the changing pore geometry complicates interpretation, the NEXAFS data does reveal a persistent anatase component (*e.g.*, ~17% after annealing to 1173K) that points to a size distribution in which, even after annealing to >1000 K, some smaller crystallites (< 14 nm) remain; these structures are challenging to resolve and quantify using SEM. Yet as a consequence of their much greater surface-to-volume ratio, these small crystallites are critical to maintaining the catalytic activity. The challenges associated with discriminating the catalytically functional population of crystallites solely with electron microscopy strongly underscore the need for NEXAFS spectroscopy as a complementary tool for the detection, characterization, and quantification of nanocrystalline deposits on very high surface area materials, such as nanoporous gold.

Summary

The catalytic performance of surface functionalized bulk nanoporous materials is intimately related to the morphology, composition, and structure of exposed surfaces. In order to assess the relative influence of these parameters, we have systematically examined the catalytic activity of a model oxide/metal hybrid system—ALD TiO_2/np-Au—as a function of annealing-induced changes in both morphology and crystallographic phase. Aerobic oxidation of CO was used as a benchmark test reaction for probing the activation of molecular oxygen—a key step in most catalytic oxidation reactions. The catalytic data is correlated with comprehensive characterization by NEXAFS spectroscopy, xSEM, TEM, XRD, and Raman spectroscopy. Maximum catalytic activity is observed after annealing the TiO_2/np-Au monolith to ~1000 K. NEXAFS analysis shows a clear and smooth variation in the predominant phase of the TiO_2 thin film; also at ~1000 K, a maxima is observed in the anatase component of the phase composition. Our microscopy results further suggest that crystallographic phase of the oxide can be correlated to the size distribution of TiO_2 crystallites. As catalytic activity is most strongly related to the size of TiO_2 crystallites, these data underscore the important correlation between TiO_2 phase and crystallite size; indeed, phase control as a proxy for size control could be a powerful means of rapid materials' synthesis feedback and optimization.

To fully leverage morphology and phase control and route to enhance performance, robust tools for characterization are required. Quantitative discrimination of TiO_2 polymorphs and detection of amorphous TiO_2 is unambiguously demonstrated with NEXAFS spectroscopy for ALD TiO_2 thin films (<10 nm thick) on np-Au monoliths. Analysis of Raman spectroscopy and XRD data collected as part of this study failed to provide quantitative information, especially for the amorphous component. These results emphasize the essential role that NEXAFS spectroscopy can play in the structural characterization of TiO_2/np-Au and possibly other similar surface functionalized nanoporous hybrids.

Methods:

Disk-shaped samples of np-Au (diameter ~5 mm, thickness 200-300 µm) with a porosity of ~ 70% were prepared by selective dissolution (dealloying) of $Ag_{0.7}Au_{0.3}$ alloy samples in concentrated nitric acid (48 hrs, ~65 wt% HNO_3) as previously described.[41] The as-prepared material has an average ligament diameter of ~50 nm (determined by geometrical evaluation) and a specific surface area of ~3.6 m^2/g. Approximately 2 nm thick amorphous TiO_2 films were deposited by 30 cycles of the titanium tetrachloride/water ($TiCl_4/H_2O$)[42] ALD process in a warm wall reactor (wall and stage temperature of 383 K). Long pulse, pump and purge times (90 s each) were used to ensure uniform coatings throughout the porous material; the chamber was isolated from the vacuum line during dosing. The growth rate per cycle (0.07 nm/cycle) was calculated from the measured mass gain and the known surface area of np-Au.

The cross-sectional scanning micrographs (xSEM) were collected with a JOEL JSM-7401F with a SEI detector and the electron probe normal incidence to the sample, using 20 µA emission current, and an accelerating voltage of 20 kV. Representative SEM micrographs were selected from at least 10 analogous images at each magnification and across each sample. The same sample series was used for NEXAFS spectroscopy measurements for consistency. For transmission electron microscopy (TEM) investigation 50 – 100 nm thin slices (cross sections) of the npAu hybrid material were prepared. First, the nanoporous gold disks were embedded in an epoxy resin for stabilization of the porous network and the gold ligaments. Subsequently, thin slices of the nanoporous gold were cut with the diamond knife of an ultra-microtome. These slices were investigated by a Tecnai F20 S-TWIN microscope (Fei) operated at 200 kV.

The effects of post-ALD annealing at 773-1273 K on phase composition of the TiO_2/np-Au hybrid material was assessed by total electron yield (TEY) near-edge x-ray absorption fine structure (NEXAFS)[33] and cross sectional scanning electron microscopy (xSEM), respectively. The Ti $L_{2,3}$-edge (455-470 eV) NEXAFS measurements were performed at beamline 8.0.1 of the Advanced Light Source, LBNL[43] using an angle of incidence of ~45°. The data were normalized to the incident x-ray flux (measured simultaneously using the drain current to an upstream gold-coated mesh inserted into the beam path), background corrected by subtraction of the pre-edge intensity, and further normalized to the magnitude of both the integrated intensity across the edge and to the absorption step, *i.e.*, the difference in absorbance between ~455 and 470 eV. Integrated intensity was used to isolate consideration of subtle higher energy peaks reported[26] in the 469 to 482 eV range that occur above the primary resonances in a regime typically preferred for step edge normalization. The overall intensity had much less impact on the analysis than line-shape and peak positions. Nonetheless, normalization to the integrated intensity provided the most consistent output. Reference samples of rutile and anatase TiO_2 (powder, 99.95%, Sigma Aldrich) were measured and correlated with literature values.[26]

The catalytic experiments were performed in a continuous flow, vertically aligned tube reactor surrounded by a tube furnace. The samples were placed on quartz wool and the temperature was measured by a thermocouple placed near the sample inside the reactor. Initial activation was performed by loading the TiO_2/np-Au samples into the preheated reactor purged with synthetic air (Linde AG, 20 % O_2, balance N_2). After annealing for 60 min, the samples were removed from the hot reactor for rapid cooling. Catalytic activity for CO oxidation of the annealed TiO_2/np-Au samples was then measured using a feed gas mixture of 12 vol% CO (Linde AG, 4.7) and 30 vol% O_2 (Linde AG, 4.5) in He (Linde AG 5.0) at total gas flow of 50 ml min^{-1} (He balanced). The gas flow was controlled by mass flow controllers (Bronkhorst

Maettig), and the CO/CO_2 product ratio was measured with online gas analyzers (URAS 10E Hartmann und Braun).

Acknowledgements:

Work at LLNL was performed under the auspices of the US DOE by LLNL under Contract DE-AC52-07NA27344. Project 13-LW-031 was funded by the LDRD Program at LLNL. NEXAFS data were acquired at beamline 8.0.1 at the Advanced Light Source, Lawrence Berkeley National Laboratory, which is supported by the Director of the Office of Science, Department of Energy, under Contract No. DE-AC02-05CH11231. AW, AW and MB thank the University Bremen for financial support within the initiative "Func-Band". We gratefully acknowledge the experimental support (SEM) of Petra Witte (Prof. Willems, Historical Geology – Paleontology, Geology department of the University Bremen).

Supporting Information Available: Output of linear combination fitting for each NEXAFS spectra, corroborative data from XRD and Raman spectroscopy, further description of morphology annealing effects with attention to mass transport and changing surface area. This material is available free of charge *via* the Internet at http://pubs.acs.org.

References:

1. A. Wittstock, V. Zielasek, J. Biener, C. M. Friend and M. Bäumer, Science **327** (5963), 319-322 (2010).
2. J. Biener, A. Wittstock, L. A. Zepeda-Ruiz, M. M. Biener, V. Zielasek, D. Kramer, R. N. Viswanath, J. Weissmuller, M. Baumer and A. V. Hamza, Nat. Mater. **8** (1), 47-51 (2009).
3. A. W. Zhu, Y. Tian, H. Q. Liu and Y. P. Luo, Biomaterials **30** (18), 3183-3188 (2009).
4. K. M. Kosuda, A. Wittstock, C. M. Friend and M. Baumer, Angew. Chem.-Int. Edit. **51** (7), 1698-1701 (2012).
5. R. Zeis, T. Lei, K. Sieradzki, J. Snyder and J. Erlebacher, J. Catal. **253** (1), 132-138 (2008).
6. S. O. Kucheyev, J. Biener, T. F. Baumann, Y. M. Wang, A. V. Hamza, Z. Li, D. K. Lee and R. G. Gordon, Langmuir **24** (3), 943-948 (2008).
7. J. L. Lu, B. S. Fu, M. C. Kung, G. M. Xiao, J. W. Elam, H. H. Kung and P. C. Stair, Science **335** (6073), 1205-1208 (2012).
8. C. T. Hsieh, W. Y. Chen, D. Y. Tzou, A. K. Roy and H. T. Hsiao, Int J Hydrogen Energ **37** (23), 17837-17843 (2012).
9. Y. C. Liang, C. C. Wang, C. C. Kei, Y. C. Hsueh, W. H. Cho and T. P. Perng, J Phys Chem C **115** (19), 9498-9502 (2011).
10. X. F. Li, X. B. Meng, J. Liu, D. S. Geng, Y. Zhang, M. N. Banis, Y. L. Li, J. L. Yang, R. Y. Li, X. L. Sun, M. Cai and M. W. Verbrugge, Adv Funct Mater **22** (8), 1647-1654 (2012).
11. A. Kudo, T. Fujita, X. Y. Lang, L. Y. Chen and M. W. Chen, Mater. Trans. **51** (9), 1566-1569 (2010).
12. X. Y. Lang, A. Hirata, T. Fujita and M. W. Chen, Nat. Nanotechnol. **6** (4), 232-236 (2011).
13. I. X. Green, W. Tang, M. Neurock and J. T. Yates, Science **333** (6043), 736-739 (2011).
14. A. Wichmann, A. Wittstock, K. Frank, M. M. Biener, B. Neumann, L. Mädler, J. Biener, A. Rosenauer and M. Bäumer, ChemCatChem **5** (7), 2037-2043 (2013).
15. J. Biener, A. Wittstock, T. F. Baumann, J. Weissmuller, M. Baumer and A. V. Hamza, Materials **2** (4), 2404-2428 (2009).
16. J. Erlebacher, M. J. Aziz, A. Karma, N. Dimitrov and K. Sieradzki, Nature **410** (6827), 450-453 (2001).
17. J. Erlebacher, J. Electrochem. Soc. **151** (10), C614-C626 (2004).
18. H. Rosner, S. Parida, D. Kramer, C. A. Volkert and J. Weissmuller, Adv. Eng. Mater. **9** (7), 535-541 (2007).
19. M. M. Biener, J. Biener, A. Wichmann, A. Wittstock, T. F. Baumann, M. Baeumer and A. V. Hamza, Nano Lett. **11**, 3085–3090 (2011).
20. L. Q. Nguyen, C. Salim and H. Hinode, Applied Catalysis A: General **347** (1), 94-99 (2008).
21. U. Diebold, Surf. Sci. Rep. **48** (5-8), 53-229 (2003).
22. Z. Y. Jiang, Q. Kuang, Z. X. Xie and L. S. Zheng, Adv Funct Mater **20** (21), 3634-3645 (2010).
23. W. F. Yan, B. Chen, S. M. Mahurin, V. Schwartz, D. R. Mullins, A. R. Lupini, S. J. Pennycook, S. Dai and S. H. Overbury, J Phys Chem B **109** (21), 10676-10685 (2005).
24. P. Guttmann, C. Bittencourt, S. Rehbein, P. Umek, X. X. Ke, G. Van Tendeloo, C. P. Ewels and G. Schneider, Nat. Photonics **6** (1), 25-29 (2012).
25. P. Kruger, Phys. Rev. B **81** (12) (2010).
26. S. O. Kucheyev, T. van Buuren, T. F. Baumann, J. H. Satcher, T. M. Willey, R. W. Meulenberg, T. E. Felter, J. F. Poco, S. A. Gammon and L. J. Terminello, Phys. Rev. B **69** (24) (2004).
27. G. S. Henderson, X. Liu and M. E. Fleet, Phys. Chem. Miner. **29** (1), 32-42 (2002).
28. V. S. Lusvardi, M. A. Barteau, J. G. Chen, J. Eng, B. Fruhberger and A. Teplyakov, Surf. Sci. **397** (1-3), 237-250 (1998).
29. Y. Hwu, Y. D. Yao, N. F. Cheng, C. Y. Tung and H. M. Lin, Nanostruct. Mater. **9** (1-8), 355-358 (1997).
30. J. G. Chen, Surf. Sci. Rep. **30** (1-3), 1-152 (1997).
31. J. P. Crocombette and F. Jollet, J. Phys.-Condes. Matter **6** (49), 10811-10821 (1994).
32. J. Biener, E. Farfan-Arribas, M. Biener, C. M. Friend and R. J. Madix, J. Chem. Phys. **123** (9), 094705 (2005).
33. J. Stöhr, *NEXAFS spectroscopy*. (Springer-Verlag, New York, 2003).

34. S. Yin, Y. Inoue, S. Uchida, Y. Fujishiro and T. Sato, Journal of Materials Research **13** (4), 844-847 (1998).
35. J. Muscat, V. Swamy and N. M. Harrison, Phys. Rev. B **65** (22) (2002).
36. A. S. Barnard and H. F. Xu, ACS Nano **2** (11), 2237-2242 (2008).
37. X. Chen and S. S. Mao, Chem. Rev. **107** (7), 2891-2959 (2007).
38. M. R. Ranade, A. Navrotsky, H. Z. Zhang, J. F. Banfield, S. H. Elder, A. Zaban, P. H. Borse, S. K. Kulkarni, G. S. Doran and H. J. Whitfield, Proc. Natl. Acad. Sci. U. S. A. **99**, 6476-6481 (2002).
39. H. Z. Zhang and J. F. Banfield, J. Mater. Chem. **8** (9), 2073-2076 (1998).
40. S. Shaikhutdinov and H. J. Freund, in *Annual Review of Physical Chemistry, Vol 63*, edited by M. A. Johnson and T. J. Martinez (Annual Reviews, Palo Alto, 2012), Vol. 63, pp. 619-633.
41. A. M. Hodge, J. Biener, J. R. Hayes, P. M. Bythrow, C. A. Volkert and A. V. Hamza, Acta Mater. **55** (4), 1343-1349 (2007).
42. J. Aarik, A. Aidla, H. Mändar and T. Uustare, Appl. Surf. Sci. **172** (1-2), 148-158 (2001).
43. J. J. Jia, T. A. Callcott, J. Yurkas, A. W. Ellis, F. J. Himpsel, M. G. Samant, J. Stohr, D. L. Ederer, J. A. Carlisle, E. A. Hudson, L. J. Terminello, D. K. Shuh and R. C. C. Perera, Rev. Sci. Instrum. **66** (2), 1394-1397 (1995).

Supporting Information for:

Quantitative Phase Composition of TiO_2-Coated Nanoporous-Au Monoliths by X-ray Absorption Spectroscopy and Correlations to Catalytic Behavior

Michael Bagge-Hansen,[1] Andre Wichmann,[2] Arne Wittstock,[2] Jonathan R. I. Lee,[1] Jianchao Ye,[1] Trevor M. Willey,[1] Juergen Biener,[1] Tony van Buuren,[1] Marcus Bäumer,[2] and Monika Biener[1]

[1]*Physical and Life Sciences Directorate, Condensed Matter and Materials Division, Lawrence Livermore National Laboratory, 7000 East Ave., Livermore, CA 94550*

[2] *University Bremen, Centre for Environmental Research and Sustainable Technology and Institute of Applied and Physical Chemistry, Leobener Strasse NW2, 28359 Bremen, Germany*

NEXAFS spectroscopy of ALD-TiO_2/Au:

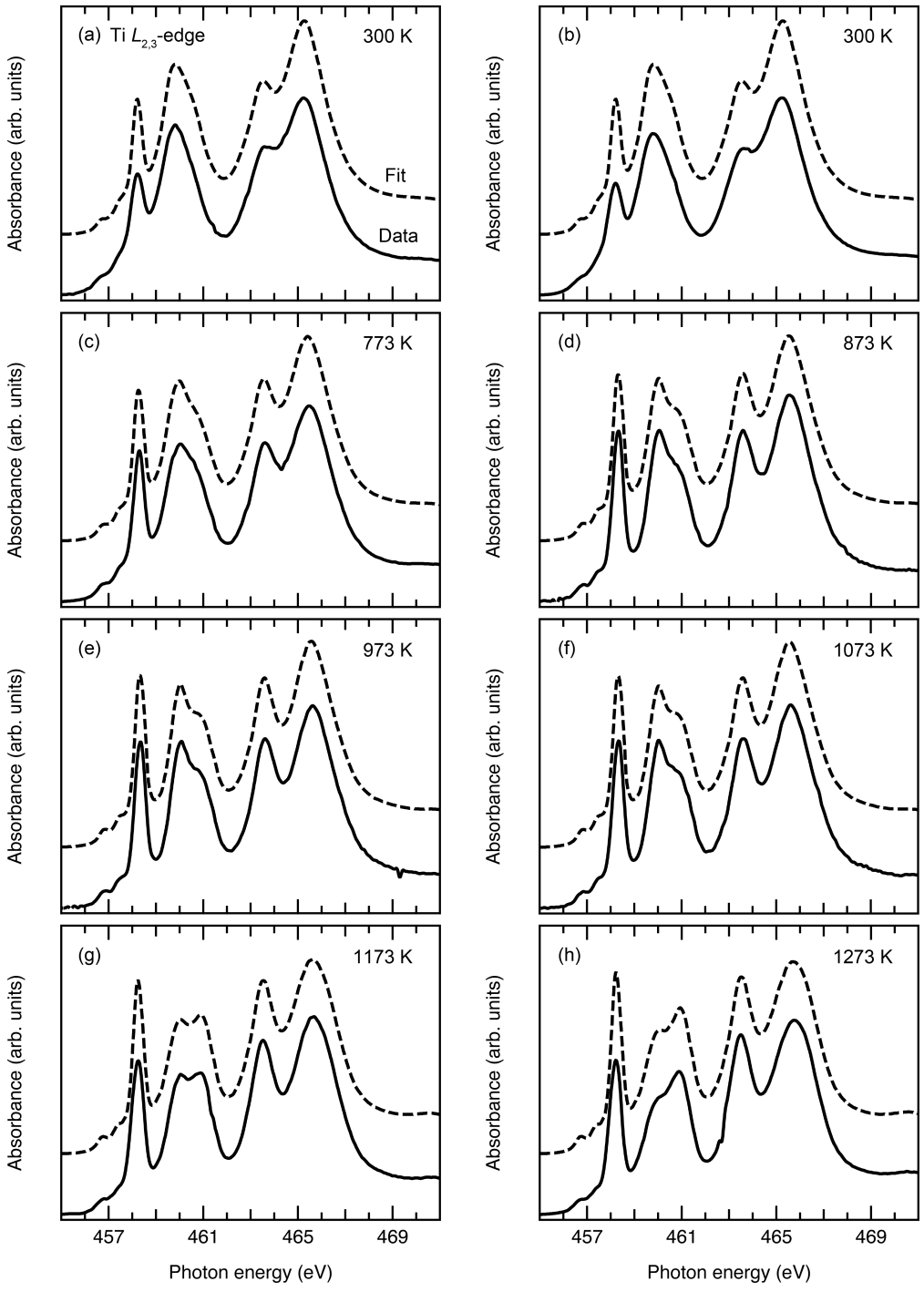

Figure S.I. -1: Comparison of acquired and simulated Ti $L_{2,3}$-edge NEXAFS spectra of TiO_2/npAu: (a-b) two separate as-deposited samples not subjected to post-annealing, (c-h) samples processed at annealing temperatures from 773 to 1273 K. Simulated spectra are output from digital linear combination fitting within a custom macro written in IGOR (WaveMetrics) . Reference spectra of amorphous, anatase, and rutile TiO_2 are the three components of the linear combination. The quality of the fits suggests that the basis set is sufficient and the inclusion of Brookite is unnecessary; however, Raman spectroscopy confirms that the Brookite phase is not present (see S.I.-2 below).

Raman spectroscopy of ALD-TiO_2/Au:

For the same series of post-ALD annealed TiO_2/np-Au investigated by NEXAFS, Raman spectra were acquired with a Thermo Electron Nicolet Almega XR Dispersive Raman spectrometer. Raman spectroscopy provided corroborative data for our NEXAFS study, but also highlights the advantages of pursuing quantitative analysis of TiO_2/np-Au using NEXAFS. The spectrometer has an instrumental resolution was about 2 cm^{-1}, with a 633 nm excitation light. The laser power was reduced to ~0.78 mW with a spot size of 1.3 µm to minimize the risk of radiation damage. (633 nm, 50X, spot size 1.3 um, 10% power (0.78 mW), 25 frames, exposure time 5 s. Three points on each sample).

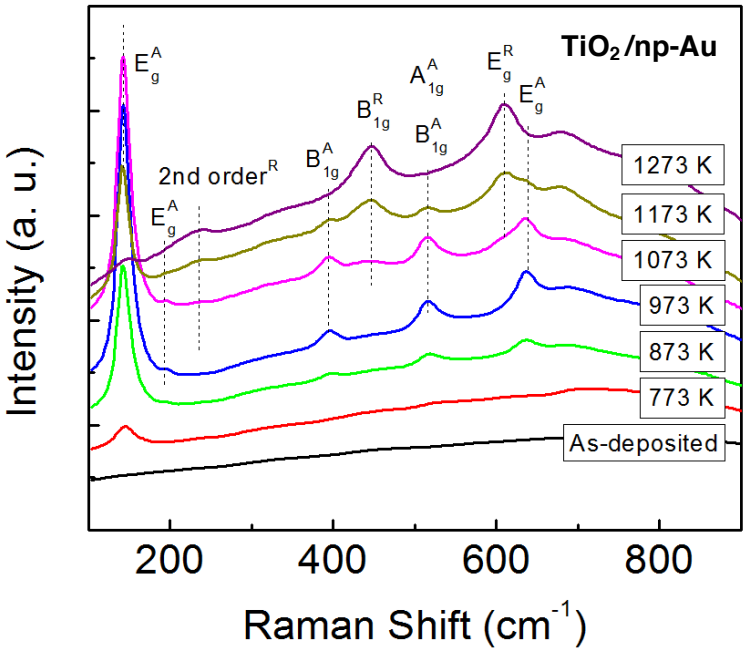

Figure S.I.-2: Raman spectra of ALD TiO_2/np-Au samples as-deposited and after post-deposition annealing to temperatures from 773-1273 K. The intense and broad backgrounds are due to the high fluorescence yield from Au. No peaks attributable to TiO_2 are observed in the as-deposited data—the absence of peaks is consistent with an amorphous TiO_2 film. Peaks associated with anatase TiO_2 are observed after annealing to 773 K; additional rutile TiO_2 peaks appear after annealing to 1173 K. No peaks associated with the brookite phase are observed.

Raman spectroscopy is a well-described approach for discerning the presence of various TiO_2 phases [ref]. The relevant TiO_2 phases and anticipated peak positions from the literature[1] follow: anatase (198, 397, 518, 638 cm^{-1}), brookite (250, 322, 636 cm^{-1}), and rutile (449, 610 cm^{-1}).

Figure S.I.-2 shows the Raman spectra of ALD TiO_2/np-Au samples as-deposited and after post-deposition annealing to temperatures from 773-1273 K. The Raman spectrum from as-deposited TiO_2/np-Au sample shows no Raman peaks, and is consistent with an amorphous TiO_2 thin film. After annealing to

[1] See, *e.g.,* M. P. Moret, R. Zallen, D. P. Vijay, and S. B. Desu, *Thin Solid Films* 366 (2000) 8-10, and references therein.

773 K, a peak emerges, E_g at 145 cm^{-1}, corresponding to the external vibration and indicates a nascent presence of the anatase TiO_2 phase. After further annealing to 873 K, this E_g peak shifts to the red, *i.e.,* 142 cm^{-1}, which may be the result of crystal growth[1]; other vibrational modes, consistent with the anatase phase, also become visible, including B_{1g} at 396 cm^{-1}, A_{1g} or B_{1g} at 515 cm^{-1}, and E_g at 639 cm^{-1}. After further annealing to 1073 K, a phase transition from anatase to rutile phase is observed, which is evinced by the emerging of B_{1g} (443 cm^{-1}), E_g (610 cm^{-1}), and 2nd order scattering (233 cm^{-1}) peaks. At 1273 K, only peaks from the rutile phase are perceptible, suggesting the majority of the TiO_2 thin film has transformed into the rutile phase. No Brookite peaks are observed in these Raman spectra.

The annealing-induced phase transitions of the ALD TiO_2 thin film observed by Raman spectroscopy are consistent with our NEXAFS results; however, the juxtaposition of these two techniques highlights some general limitations to the application of Raman spectroscopy to these material systems. First, Raman scattering is very sensitive to the crystallinity and microstructure of the material. Consequently, Raman peaks become weak and broad in the presence of local lattice imperfections, so much so that in amorphous materials, no Raman peaks can be detected—as demonstrated in figure S.I.-2. Moreover, Raman scattering signals are often swamped or obscured by the background due to the intense fluorescence from, for example, organic molecules or metals (in our case, Au). This highly sample-dependent background obfuscates robust quantitative analysis. Indeed, there are few successful reports of Raman spectroscopy applied to the quantitative phase composition of TiO_2 mixtures.

XRD of ALD-TiO_2/Au:

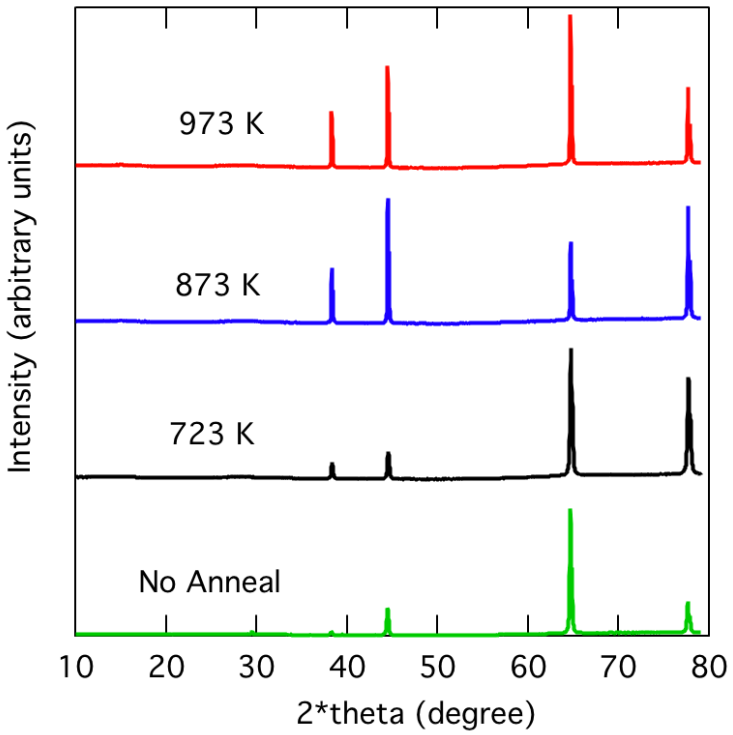

Figure S.I.-3: X-ray diffraction data from four annealed TiO_2/np-Au samples. In all cases, only diffraction peaks associated with crystallographic phases of Au are observed; no signal is detected from the ALD-TiO_2 thin film.

Coarsening of TiO_2 crystallites:

During the course of post-ALD annealing, TiO_2 likely remains at the surface; moreover, mass is conserved as dissociation, desorption or incorporation of TiO_2 are unlikely at these temperatures and pressures. As such, the total volume of TiO_2 is presumed constant; although, the number and size of crystallites changes.

The exposed TiO_2/Au interface, at the perimeter of each crystallite, is critical for catalytic activity. We can make a simple geometry argument to assess the rate of change of the total crystallite perimeter based on the mean crystallite radius, independent of phase change.

Assuming that each crystallite is approximately hemispherical, at temperature, T_i, we have the volume, V, for N_i hemispherical crystallites with radius r_i:

$$V = N_i \cdot \left[\frac{2}{3} \cdot \pi \cdot {r_i}^3\right]$$

and the associated total perimeter length X_i:

$$X_i = N_i \cdot 2 \cdot \pi \cdot r_i$$

Thus, at two different temperatures, over which crystallite size grows, we can evaluate algebraically the relationship between the change in mean radius and the associated total perimeter length:

$$\frac{X_2}{X_1} = \left[\frac{r_1}{r_2}\right]^2$$